

# RSC Advances



This is an *Accepted Manuscript*, which has been through the Royal Society of Chemistry peer review process and has been accepted for publication.

*Accepted Manuscripts* are published online shortly after acceptance, before technical editing, formatting and proof reading. Using this free service, authors can make their results available to the community, in citable form, before we publish the edited article. This *Accepted Manuscript* will be replaced by the edited, formatted and paginated article as soon as this is available.

You can find more information about *Accepted Manuscripts* in the [Information for Authors](#).

Please note that technical editing may introduce minor changes to the text and/or graphics, which may alter content. The journal's standard [Terms & Conditions](#) and the [Ethical guidelines](#) still apply. In no event shall the Royal Society of Chemistry be held responsible for any errors or omissions in this *Accepted Manuscript* or any consequences arising from the use of any information it contains.

## Electrical transport and mechanical properties of thermoelectric tin selenide

Kriti Tyagi<sup>a,b</sup>, Bhasker Gahtori<sup>a,1</sup>, Sivaiah Bathula<sup>a</sup>, Niraj Kumar Singh<sup>a</sup>, Swati Bishnoi<sup>a,b</sup>, S. Auluck<sup>a</sup>, A. K. Srivastava<sup>a</sup> and Ajay Dhar<sup>a,1</sup>

<sup>a</sup>CSIR-Network for Solar Energy, CSIR-National Physical Laboratory, Physics of Energy Harvesting Division, Dr. K. S. Krishnan Road, New Delhi – 110012, India

<sup>b</sup>Academy of Scientific and Innovative Research (AcSIR), CSIR-NPL Campus, New Delhi- 110012, India

Motivated by the unprecedented thermoelectric performance of SnSe, we report its band structure calculations, based on density functional theory using the full potential linearized augmented plane wave. These calculations were further extended to evaluate the electrical transport properties using Boltzmann transport theory and the results were compared with the as-synthesized polycrystalline counterpart, which was synthesized employing conventional vacuum melting technique followed by consolidation employing spark plasma sintering. The as-synthesized SnSe was thoroughly characterized employing XRD, FESEM and TEM for phase purity, morphology and structure. The theoretically predicted band gap values and the temperature dependence of electrical transport properties of SnSe were in reasonable agreement with the experimental results, within the approximations employed in our theoretical calculations. These theoretical calculations suggested that the optimum thermoelectric performance in SnSe is expected to occur at a hole doping concentration of  $\sim 3 \times 10^{21} \text{ cm}^{-3}$ . The measured fracture toughness and hardness of SnSe were found to be  $\sim 0.76 \pm 0.05 \text{ MPa}\sqrt{\text{m}}$  and  $0.27 \pm 0.05 \text{ GPa}$ , respectively, which are comparable with other state-of-the-art thermoelectric materials. The high value of thermal shock resistance  $\sim 252 \pm 9 \text{ W/m}$ , coupled with its good mechanical properties suggests SnSe to be a potential material for thermoelectric device applications.

**Keywords:** tin selenide, density functional theory, thermoelectric performance, mechanical properties.

---

<sup>1</sup> Corresponding author email: [adhar@nplindia.org](mailto:adhar@nplindia.org); [bhasker@nplindia.org](mailto:bhasker@nplindia.org)  
Tel. : +91 11 4560 9455/9456; Fax: +91 11 4560 9310

## 1. Introduction

Thermoelectric (TE) materials are currently being vigorously explored as a source of green energy generation from waste-heat.<sup>1,2</sup> The thermoelectric figure-of-merit ( $ZT$ ), which is a material based property, is a direct measure of its thermoelectric performance which is given as<sup>1</sup>,  $ZT = (S^2\sigma/\kappa)T$ , where  $S$  is Seebeck coefficient,  $\sigma$  is the electrical conductivity and  $\kappa$  the total thermal conductivity. Currently the thrust of thermoelectric research is on developing thermoelectric materials with a high  $ZT$  in order to increase the efficiency of their devices so that they can compete with other existing green sources of energy.<sup>1,3</sup>

The anisotropy in TE properties has been well documented on several alloys and compounds and originates primarily due to a variation in their electrical and thermal transport properties when measured along different crystallographic axes<sup>4-6</sup>. It manifests itself in terms of different TE performance, when  $ZT$  is measured in different directions in a TE sample. This anisotropy in polycrystalline materials mostly arises by using the secondary material processing techniques such as the hot pressing<sup>7,8</sup>, spark plasma sintering<sup>4,9,10</sup> and extrusion<sup>11</sup> of powdered TE material. An example of this kind of large anisotropy has recently been reported in a simple binary compound, SnSe, by Zhao et al.<sup>5</sup>, where a vastly different  $ZT$  has been observed along the different crystallographic directions. These authors have reported a very high  $ZT$  of 2.6 along the b-axis in SnSe single crystals and 2.3 and 0.8 along the c and a-axis, respectively. Although these authors report a large  $ZT$  in single crystalline SnSe along its b-axis, but its value in polycrystalline SnSe has been reported to be only 0.3<sup>12</sup>.

SnSe has a layered structure and crystallizes in orthorhombic symmetry with a space group  $Pnma$  (space group No.63) and undergoes a phase transition above a temperature of 750K, where it possesses a lower symmetry ( $Cmcm$  space group No.62). Recently, there has been a resurgence in the interest on the TE properties of SnSe<sup>5, 12-14</sup> ever since Zhao et al.<sup>5</sup> reported an unprecedented  $ZT \sim 2.62$  at 923K along its b-axis. These authors have experimentally found

its electrical and thermal transport properties to be highly anisotropic along all the crystallographic directions. Later, Sassi et. al.,<sup>14</sup> reported a ZT of 0.5 at 823K in polycrystalline SnSe, synthesized employing vacuum encapsulation followed by spark plasma sintering. Recently, Chen et al.,<sup>12</sup> have reported an enhanced ZT value of 0.6 at 750 K in melt-grown Ag doped polycrystalline SnSe.

Several authors<sup>15-19</sup> have reported the band structure of SnSe based on *ab initio* electronic structure calculations, employing different approximations. He et al.<sup>13</sup> have calculated the band structure of SnSe using the generalized gradient approximation (GGA+U) method, as applied in Vienna *ab initio* Simulation Package (VASP), and reported an indirect band gap of 0.8eV. Shi and Kioupakis<sup>15</sup> have also performed the band structure calculations of SnSe and obtained a gap of 0.829eV. Employing the first principle calculations using local density approximations (LDA), Kutorasinski et al. have reposted a band gap of 0.465eV<sup>16</sup>, however, Ding et al.<sup>17</sup> have obtained a lower band gap of 0.69 eV, calculated using the GGA approximations.

In the present work, we report the theoretically derived electrical transport properties of SnSe, calculated using density functional theory (DFT), which has been compared with those measured experimentally on as-synthesized polycrystalline SnSe. The band structure calculations have been performed using full-potential linearized augmented plane wave (FP-LAPW) as implemented in WIEN2K code, based on DFT and a band gap value of 0.89 for *Cmcm*-phase has been realized, which is in closest agreement thus far with the reported optical band gap<sup>5, 18</sup>. The band structure calculations were then extended to theoretically evaluate the electrical transport properties of SnSe, employing the Boltzmann transport theory. The results suggest that the experimentally determined temperature dependent electrical transport behavior agrees well with that predicted theoretically using density-functional theory calculations, employing Engel-Vosko Generalized Gradient Approximation (EVGGA). In addition to the TE performance, the mechanical properties of TE materials are equally important especially during actual device

operation. Thus, in the current study, we also report the hardness, fracture toughness and thermal shock resistance of as-synthesized polycrystalline SnSe.

## 2. Experimental Details

Elemental Sn and Se powders supplied by Alfa Aesar, both with a purity of 99.99%, were used as starting materials in this study. Polycrystalline SnSe was synthesized employing conventional vacuum melting process. The Sn and Se powders in a chemical stoichiometric ratio were thoroughly ground in a glove-box under a high-purity argon atmosphere and the resulting powders were subsequently pelletized and vacuum-sealed ( $10^{-5}$  Torr) in quartz tubes. The sealed quartz ampoules were heat-treated at 773K for 96h, and then naturally cooled to room temperature. The powders of bulk SnSe were subsequently consolidated and sintered under vacuum ( $\sim 4$  Pa) using spark plasma sintering (SPS Syntex,725) at optimized process parameters of pressure 60 MPa and temperature 773K for 2min (soaking time) at a heating rate of 200°C/min using graphite die and punches. The density was measured using the conventional Archimedes principle and was found to be 99.2% of the theoretical density. Phase identification and crystallite size measurements were carried out using Rigaku powder XRD (40 kV and 30 mA) and the data was acquired at a scanning speed of 0.51/min with a step width of 0.051. High resolution transmission electron microscopy (HRTEM, model Technai G2 F30 STWIN with a field emission electron gun and operated at 300 kV electron accelerating voltage) was performed on spark plasma sintered (SPS) SnSe. Electrical properties measurements were performed employing ULVAC - ZEM 3 system with an average sample dimensions 2 x 2 x 8 mm. Indentation-crack technique was employed for estimating the fracture toughness using Vickers micro-hardness tester (FM-e7) with a load of 0.98 N for 10 s of indentation time. Field Emission Scanning Electron Microscope (FESEM) - Supra 40VP has been used to study the surface morphology of as-synthesized samples. Fracture tests of the sample have been performed at

room temperature using Instron (4204) as per ASTM standard (ASTM: E9-09) with an aspect ratio of  $\sim 2.5$  under uniaxial compressive loading with a strain rate of  $2 \times 10^{-5} \text{ s}^{-1}$ .

### 3. Computational Details

The FP-LAPW<sup>19</sup> method in a scalar relativistic version, based on DFT<sup>20</sup> as implemented in WIEN2K code, was employed to perform theoretical band structure calculations<sup>21</sup>. The atomic coordinates of SnSe were optimized by minimizing the forces acting on each atom. Employing GGA, as given by Perdew-Burke-Ernzerhof<sup>22</sup>, we assume that the structure is fully relaxed when the forces on the atoms reach values less than 1 (mRy/a.u.). Once the forces are minimized in this construction, the self-consistent density at these positions is determined by turning off the relaxations and driving the system to self-consistency. From the relaxed geometry thus obtained, the electronic structure, chemical bonding and electronic charge density were calculated and these were then used to evaluate the transport properties followed by their comparison with the experimentally measured data.

The theoretical calculation were performed using the DFT within the FP-LAPW method in a scalar relativistic version as embodied in the WIEN2k code<sup>16, 21</sup>. The exchange-correlation (XC) potential was solved using three different possible approximations. The XC was described by the LDA and the GGA, which is based on exchange-correlation energy optimization to calculate the total energy<sup>22, 23</sup>. In addition, we have also used EVGGA<sup>24</sup>, which optimizes the corresponding potential for electronic band structure calculations.

It is well-known that in calculating the self-consistent band structure within DFT, the LDA approximation generally underestimates the band gap<sup>25</sup>. This is mainly due to the fact that LDA has relatively simple forms that are not sufficiently flexible to accurately reproduce both the exchange–correlation energy and its charge derivative. Engel and Vosko<sup>24</sup> considered this shortcoming and constructed a new functional form of GGA that is able to better reproduce the

exchange potential at the expense of lesser agreement in with the exchange energy. This approach yields better band splitting and some other properties that mainly depend on the accuracy of the exchange–correlation potential.

The Kohn-Sham equations were solved using a basis of linear augmented plane wave. The potential and charge density in the muffin-tin (MT) spheres are expanded in spherical harmonics with  $l_{max}=10$  and non-spherical components up to  $l_{max}=4$ . We have used  $R^*K_m=7.0$ . In the interstitial region the potential and the charge density are represented by Fourier series. Self-consistency is obtained using 360k points in the irreducible Brillouin zone (IBZ). The self-consistent calculations converge since the total energy of the system is stable within 0.00001Ry. We extended our DFT studies to calculate the transport properties using 9900 k points in IBZ, which were calculated employing Boltzmann theory with constant scattering time approximation (CSTA) as implemented in the BoltzTraP code<sup>26-28</sup>. The CSTA was used to directly calculate the Seebeck coefficient as a function of doping level and temperature, with no adjustable parameters<sup>29, 30</sup>.

## 4. Results and Discussion

### 4.1 Microstructural Characterization

The X-ray diffraction data of the as-synthesized polycrystalline SnSe sample is shown in Fig. 1 (a). The XRD pattern can be indexed to the orthorhombic phase of SnSe and the calculated lattice parameters  $a = 1.15$  nm,  $b = 0.416$  nm,  $c = 0.443$  nm are in good agreement with those reported in the literature<sup>14, 31</sup>. The sharpness in the peaks in the XRD pattern indicates the highly crystalline behaviour and the absence of other residual peaks in the spectrum exhibits phase purity of the as-synthesized SnSe sample. The average crystallite size of the as-synthesized SnSe was determined using Williamson-Hall method and was found to be  $\sim 42$  nm. Fig. 1(b) shows the surface morphology of as-synthesized polycrystalline SnSe, elucidated employing FESEM. It is apparent from the figure that the microstructure exhibits nearly equiaxed na-

nanoscale grains with an average grain size of 40 – 50 nm, which is in close agreement with that evaluated employing XRD data. Also, the crystallite size distribution graph has been shown in inset of Fig. 1(b).

A detailed electron microscopy in real and reciprocal space led to important information pertaining to ultra-fine microstructural evolution in the material. Figure 2(a) shows an illustrative micrograph of fine grains with uniform distribution and densely packed throughout in the microstructure. A corresponding selected area electron diffraction pattern (SAEDP, inset A in Fig. 2(a)) exhibits a polycrystalline nature of the material with the Debye rings, revealing three important atomic planes of the interplanar spacings of 0.293, 0.287, 0.183 nm with respective hkl indices of 111, 400, 511, of an orthorhombic crystal structure (space group: Pnma, lattice parameters:  $a = 1.15$ ,  $b = 0.42$ ,  $c = 0.44$  nm, reference: ICDD, 00-014-0159). The ultrafine crystallites of nano-grained microstructure further exhibits that these in most of the instances the thin crystals are overlapping and therefore elucidating the presence of moiré fringes. Inset B in Fig. 2(a) shows a set of almost parallel translational - moiré patterns with a fringe spacing of about 1.13 nm between them. Underneath of these moiré fringes a stacking of high index atomic planes with interplanar spacing of about 0.183 nm (hkl: 511) are also depicted in the inset B of Fig. 2(a). Fig. 2(b) clearly displays that the intrinsically formed individual nanograins are faceted and ultrafine with the size approximately between 30 to 60 nm. At the atomic scale, a grain with size about 40 nm (Fig. 2(b)), shows a distinct stacking of planes with the interplanar spacing of about 0.287 nm of corresponding hkl: 400 (inset C in Fig. 2(b)), in correspondence with XRD and FESEM data. The interfaces between these nanograins were also examined under the electron beam to look into the microstructure. Inset A in Fig. 3 shows an interface (marked with a set of arrows) constituted between the two grains I and II. A further magnified area of encircled region in inset A of Fig. 3 with white dotted line reveal the thickness of the interface about 2 nm stacked between grains I and II (inset B of Fig. 3). Moreover, at the apex of the interface, the microstructure was mixed with the existence of both dis-

torted atomic planes and amorphous phase (inset B of Fig. 3). However the high resolution images of either sides of interface shows single crystalline nature. As an illustrative example, in Fig. 3, a single grain II shows the presence of well stacked atomic planes with the interplanar spacing of 0.293 nm of hkl indices 111.

#### 4.2 Band structure calculations

The band structure of SnSe (*Cmcm* phase), within a few eV from the Fermi level, is shown in Fig. 4(a) (Supplementary information<sup>42</sup> Fig. S1(a) for *Pnma* phase). The valence band maxima as well as the conduction band minima, along X -  $\Gamma$  direction in the band structure, suggests a direct energy band gap of 0.89 eV, which has also been substantiated experimentally employing UV absorption spectroscopy (Figure S2). This band gap is in close agreement with that reported earlier from optical absorption measurements (0.898 eV).<sup>5, 18</sup> The nature of band structure for both the phases of SnSe is similar to that reported by He et al.<sup>13</sup>, calculated using VASP. Shi et al.<sup>15</sup> have reported a band gap value of 0.829 eV for the *Pnma* phase, 0.46 eV for the *Cmcm* phase of SnSe, employing the plane wave pseudo potential model. Kutorasinski et al.<sup>16</sup> employed LDA approximation and reported a band gap of 0.465 eV for *Pnma* and 0.355eV for *Cmcm* phase. In yet another study, using the GGA approximation, Ding et al.<sup>17</sup> have obtained a band gap of 0.69 eV in *Pnma* phase, while recently, Zhao et al.<sup>5</sup> have reported an indirect band gap of 0.86 eV for the low temperature *Pnma* phase of SnSe. Thus the band gap values, evaluated in the current study using full-potential WIEN2K code, gives the closest agreement with experimentally determined values, compared to other reported studies<sup>15-18</sup>.

Fig. 4(b) shows the contribution of each atom to the density of states (DOS) for the *Cmcm* phase, via partial-DOS, which clearly shows a finite gap between valance and conduction band (Supplementary information<sup>42</sup> Fig. S1(b) for *Pnma* phase). The valence band comprises of peaks at around -7.5eV and between 0 and -5eV. The peak around -7 eV arises from the s-state of Sn. The top of the valence band has major contributions from Sn-p, Se-p and Sn-s while the

bottom of the conduction band arises from Sn-p and Se-p states. We find a significant hybridization between Sn-p, Se-p and Se-d from -5.0 eV to top of valence bands. Conduction band mainly comprises of Sn-p and Se-d states. The inset of Fig 4(b) shows an enlarged axial view of the partial DOS for *Cmcm* phase of SnSe, within a few eV from the Fermi level.

### 4.3 Electrical Transport

Fig. 5 shows the temperature dependence of Seebeck coefficient and electrical conductivity of *Pnma* and *Cmcm* phases of SnSe along the three crystallographic directions for both hole (p-type) and electron (n-type conduction), calculated using BoltzTrap code<sup>26</sup>, over the temperature range of 300 - 850K. Hole or electron conduction was obtained by shifting the Fermi level to just below the top of valence band or just above the bottom of conduction band, respectively. It is apparent from these figures that, both, the Seebeck coefficient and electrical conductivity exhibit a strong anisotropy along the three crystallographic axes, for both the phases of SnSe, although, the anisotropy in Seebeck coefficient is comparatively large. These results are in qualitative agreement with the earlier reported experimental<sup>5, 32</sup> and theoretical studies on SnSe<sup>6, 14, 15</sup>.

Fig. 5 (a) shows comparison between the experimentally determined Seebeck coefficient for polycrystalline SnSe with those calculated theoretically along the three crystallographic axes. The experimentally determined positive values of Seebeck coefficient (Fig. 5(a)) indicates a p-type conductivity its temperature dependence is reasonably in close agreement to those calculated theoretically, in the *Pnma* phase of SnSe. The discontinuity at ~ 450 K is accounted to the thermal activation of the carriers<sup>5</sup> while at ~750K corresponds to the phase transition from *Pnma* to *Cmcm* space group<sup>5</sup>. This temperature dependence of Seebeck coefficient (Fig 5(a)) is also similar to those reported experimentally by Sassi et al.<sup>14</sup> and Zhao et al.<sup>5</sup> However, for *Cmcm* phase, a mixture of light and heavy conduction bands could explain a nearly temperature independent thermopower owing to bipolar conduction<sup>19</sup>.

Fig. 5(b) shows that the experimental electrical conductivity increases with temperature although this increase is much sharper in *Cmcm* phase. In contrast, the theoretically estimated temperature dependence of conductivity of SnSe (p-type) reveals nearly a linear behaviour with a negative slope. This could be attributed to the fact that a constant scattering time ( $\tau$ ) approximation has been used to theoretically evaluate the electrical conductivity using DFT, while in practice  $\tau$  varies with temperature, hence the observed deviation in experimental and theoretical behaviour of electrical conductivity. Moreover, DFT is known to underestimate the band gap of semiconductors and insulators when using local and semi-local approximation. Hence, SnSe, with a band gap of  $\sim 0.8$  eV behaves as metal while performing transport properties calculations using DFT, which is clearly reflected in temperature dependence of electrical conductivity as the theoretically calculated values decrease continuously with temperature in the entire temperature. Despite these limitations, both the calculated and experimental electrical conductivity values lie in same range. In view of various approximations that have been applied in the theoretical calculations, the agreement between experiment and theoretical behaviour of electrical properties of SnSe is quite reasonable. The dependence of power factor (PF) with temperature is also depicted in Fig. 5 (c). A strong variation along y-axis as compared to x- and z-axis, in the entire temperature range is observed, which is well in accordance with the results shown in Figs. 5 (a) and (b). A slope change at  $\sim 750$  K in the experimental results and theoretical calculations indicates the discussed phase transition.

To get a better understanding of the transport phenomenon in SnSe, the Boltzmann transport calculations for the Seebeck coefficient (S), electrical conductivity with respect to relaxation time ( $\sigma/\tau$ ) and power factor with respect to relaxation time ( $S^2\sigma/\tau$ ) as a function of carrier concentration were carried out. The behaviour of S,  $\sigma/\tau$  and  $S^2\sigma/\tau$ , as a function of carrier concentration, along the three crystallographic axes for both the phases of SnSe, are depicted in Fig. 6 (a-f). Figures 6 (a) and (b) show that S decreases with increasing carrier concentration in accordance with the “Pisarenko Relation” for both the phases. This decrease in S, for both *Pnma*

and *Cmcm* phases, is nearly similar along x- and z-axis however in contrast along the y-axis it shows a lower S till a carrier concentration of  $\sim 2 \times 10^{21} \text{ cm}^{-3}$  after which a broad hump is observed. This suggests that the magnitude of the Seebeck coefficient can be tailored suitably by tuning the carrier concentration. The carrier concentration dependence of  $\sigma/\tau$  is shown in Figs. 6 (c) and (d) for *Pnma* and *Cmcm* phases of SnSe, respectively. These figures suggest that the *Cmcm* phase exhibits higher values of  $\sigma/\tau$  as compared to *Pnma* phase. Although, while for *Pnma* phase,  $\sigma/\tau$  exhibits almost similar behaviour in all the three crystallographic directions, the anisotropy is clearly pronounced in the case of *Cmcm* phase. Owing to the different trend in variation of S and  $\sigma/\tau$  along the three axis, the  $S^2\sigma/\tau$  values for *Pnma* phase show a strong variation with carrier concentration, along all the three axes, as compared to *Cmcm* phase (Figures 6 (e) and (f)). Typically, in the *Pnma* phase along y-axis,  $S^2\sigma/\tau$  value decreases till a carrier concentration of  $\sim 2 \times 10^{21} \text{ cm}^{-3}$  (Fig. 6(e)) after which S starts to increase with temperature (Fig. 6 (a)) leading to an overall increase of  $S^2\sigma/\tau$  values. Similar to S and  $\sigma/\tau$ , the graph for  $S^2\sigma/\tau$  *Cmcm* phase (Fig. 6(f)) shows a strong variation along y-axis as compared to x- and z-axis, in the entire temperature range. The magnitude of  $S^2\sigma/\tau$  along y-axis is  $\sim 8$  times lower than x- and z- axis. For both the phases, a peak value of  $S^2\sigma/\tau$  occurs at a carrier concentration of  $\sim 3 - 5 \times 10^{21} \text{ cm}^{-3}$ , where the bipolar effect is clearly evident. Fig. 6 (f) clearly shows that  $S^2\sigma/\tau$  would show a maximum value at a hole doping concentration of  $\sim 3 - 5 \times 10^{21} \text{ cm}^{-3}$  which qualifies as an optimum condition for ideal TE performance in *Cmcm* phase of p-type SnSe.

#### 4.4 Mechanical properties

Most of the research on TE materials has been focused only on their thermal and electrical transport properties<sup>12, 29, 33-38</sup>, primarily aimed towards enhancing their TE performance<sup>9</sup>. Nevertheless, their mechanical properties are also equally important the long term durability of the TE devices, as the TE materials, in general, are known to be brittle with low fracture toughness<sup>39</sup>. The hardness values of the as-synthesized polycrystalline SnSe, measured using Vick-

ers indentation method at a load of 0.98 N with a dwell time of 10 sec, was found to be  $0.27 \pm 0.05$  GPa. The relatively low hardness value of SnSe was attributed to its brittle nature coupled with its bulk to shear modulus ratio which is less than  $1.75^{13}$ . The fracture toughness ( $K_{IC}$ ) of brittle materials was estimated using Vicker's indentation-crack technique, given by Antis *et al.*<sup>40</sup> for radial mean crack systems:

$$K_{IC} = 0.016 \left( \frac{E}{H} \right)^{1/2} \times \frac{P}{c^{3/2}} \dots\dots\dots(1)$$

where,  $P$  is the load,  $c$  is the half-diagonal of Vicker's indentation mark in meters,  $E$  is Young's modulus  $65.7$  GPa<sup>13</sup> and  $H$  is Vickers hardness  $\sim 0.27 \pm 0.05$  GPa. FESEM was employed for measuring the crack lengths to estimate the fracture toughness which was found to be  $0.76 \pm 0.05$  MPa $\sqrt{m}$ , employing equation (1). This value is comparable to those reported for other commercial TE materials, including PbTe<sup>41</sup> and Bi<sub>2</sub>Te<sub>3</sub><sup>39</sup>. The thermoelectric compatibility factor of a TE material is defined as<sup>42</sup>,

$$\alpha = \frac{\sqrt{1 + ZT} - 1}{ST} \dots\dots\dots(2)$$

where  $S$  is Seebeck coefficient in Volts,  $T$  is temperature in Kelvin. The compatibility factor for any given material for segmentation is to be less than a factor of 2 is required for better power output. The compatibility factor of as-synthesized SnSe, calculated using equation (2), was found to be 0.68 at 773 K (Supplementary information<sup>42</sup> Fig. S3). In the mid-temperature range p-type TE materials, such as, MnSi<sub>2</sub><sup>43</sup>, PbTe<sup>43</sup>, Cu<sub>2</sub>Se<sup>44</sup>, half-hausler alloys<sup>43</sup> and other TE materials<sup>45</sup> have a compatibility factor of  $< 2$ , thus making these TE materials suitable for segmentation with SnSe for enhancing their TE performance.

The magnitude of thermal shock resistance for TE materials is very important parameter during actual operation of the device, owing to the temperature gradient between the hot and cold ends of the TE device legs, which can lead to material failure due to internal mechanical stress in-

duced by the temperature gradients<sup>46-48</sup>. The thermal shock resistance parameter ( $R_T$ ), is given by the expression<sup>46</sup>,

$$R_T = \frac{\sigma(1-\nu)\kappa}{\alpha E} \dots\dots\dots(3)$$

where,  $\nu$  is Poisson's ratio,  $\kappa$  is thermal conductivity and  $\alpha$  is the coefficient of thermal expansion,  $\sigma$  is fracture strength and  $E$  is Young's modulus. The value  $R_T$  for SnSe was estimated using equation (3) employing experimentally determined values of  $\sigma=0.07$  GPa,  $\kappa=0.88$  W/mK,  $\alpha=2.45 \times 10^{-5}/K^{13}$  and  $\nu=0.22^{13}$ ,  $E=65.7$  GPa<sup>13</sup> from the literature. The estimated value of  $R_T$  was found to be  $\sim 252 \pm 9$  Wm<sup>-1</sup> which is much higher than most state-of-the-art TE material<sup>44, 49, 50</sup>.

### Conclusions

The theoretically evaluated temperature dependence of electrical transport properties in SnSe, calculated using first-principle density functional theory and Boltzmann transport equations, have been compared with those measured experimentally on as-synthesized polycrystalline SnSe. These results suggest a reasonable agreement of the theoretically derived band gap and temperature dependence of electrical conductivity and Seebeck coefficient with the experimentally measured values, within the approximations employed in our theoretical calculations. These theoretical calculations suggests that the optimum thermoelectric performance in SnSe is expected to occur at a hole doping concentration of  $\sim 3-5 \times 10^{21}$  cm<sup>-3</sup>. The mechanical properties of as-synthesized SnSe, including fracture toughness, hardness, fracture strength and thermal shock resistance exhibits values which are comparable to those reported for other state-of-the-art thermoelectric materials.

### Acknowledgements

This work was supported by CSIR-TAPSUN (CSIR-NWP 54) programme entitled “*Novel approaches for solar energy conversion under technologies and products for solar energy utilization through networking*”. The authors are grateful to Mr. Radhey Shyam and Mr. Naval Kishore Upadhyay for the experimental support.

**Figure captions:**

Figure 1: As-synthesized polycrystalline SnSe (a) X-ray diffraction data (b) FESEM micrograph showing inherent nanoscale microstructure. Inset in Fig.1(b) showing the crystalline size distribution.

Figure 2: HRTEM images of spark plasma sintered SnSe showing (a) ultra-fine distribution of grains, and (b) magnified view of individual grains. Insets: (A) selected area electron diffraction pattern, (B) moiré patterns along with atomic planes, and (C) atomic planes at lattice scale.

Figure 3: HRTEM images of spark plasma sintered SnSe showing the presence of atomic planes at lattice scale throughout in the microstructure. Insets: (A) interface between grains I and II, and (B) atomic scale image of the same interface as in inset A.

Figure 4: (a) Electronic band structure for *Cmcm*-phase of SnSe. The Fermi level is indicated by  $E_F$ , (b) Partial density of states for *Cmcm* phase of SnSe.

Figure 5: Temperature dependence of theoretically calculated transport properties along the crystallographic axes for SnSe (a) Seebeck coefficient (b) Electrical conductivity and (c) Power Factor.

Figure 6: Theoretically calculated carrier concentration dependence of electrical transport coefficients of *Pnma* and *Cmcm*-phases of SnSe. (a & b) Seebeck coefficient, (c & d) electrical conductivity with respect to relaxation time ( $\sigma/\tau$ ) and (e & f) power factor with respect to relaxation time ( $S^2\sigma/\tau$ ).

**References:**

1. D. M. Rowe, *Thermoelectrics handbook: macro to nano*, CRC press, 2005.
2. G. J. Snyder and E. S. Toberer, *Nature materials*, 2008, 7, 105-114.
3. D. M. Rowe, *Modules, systems, and applications in thermoelectrics*, CRC Press, 2012.
4. S. D. Bhamre, D. Pravarthana, W. Prellier and J. G. Noudem, *Applied Physics Letters*, 2013, 102, 211901.
5. L.-D. Zhao, S.-H. Lo, Y. Zhang, H. Sun, G. Tan, C. Uher, C. Wolverton, V. P. Dravid and M. G. Kanatzidis, *Nature*, 2014, 508, 373-377.
6. A. Hong, L. Li, H. Zhu, Z. Yan, J. Liu and Z. Ren, *Journal of Materials Chemistry A*, 2015.
7. S. R. Brown, S. M. Kauzlarich, F. Gascoin and G. J. Snyder, *Chemistry of materials*, 2006, 18, 1873-1877.
8. A. Zevalkink, W. G. Zeier, G. Pomrehn, E. Schechtel, W. Tremel and G. J. Snyder, *Energy & Environmental Science*, 2012, 5, 9121-9128.
9. K. Biswas, J. He, I. D. Blum, C.-I. Wu, T. P. Hogan, D. N. Seidman, V. P. Dravid and M. G. Kanatzidis, *Nature*, 2012, 489, 414-418.
10. D. Medlin and G. Snyder, *Current Opinion in Colloid & Interface Science*, 2009, 14, 226-235.
11. R. Martin-Lopez, A. Dauscher, H. Scherrer, J. Hejtmanek, H. Kenzari and B. Lenoir, *Applied Physics A*, 1999, 68, 597-602.
12. C.-L. Chen, H. Wang, Y.-Y. Chen, T. Day and G. J. Snyder, *Journal of Materials Chemistry A*, 2014, 2, 11171-11176.
13. X. He, H. Shen, W. Wang, Z. Wang, B. Zhang and X. Li, *Journal of Alloys and Compounds*, 2013, 556, 86-93.
14. S. Sassi, C. Candolfi, J.-B. Vaney, V. Ohorodniichuk, P. Masschelein, A. Dauscher and B. Lenoir, *Applied Physics Letters*, 2014, 104, 212105.
15. G. Shi and E. Kioupakis, *Journal of Applied Physics*, 2015, 117, 065103.
16. K. Kutorasinski, B. Wiendlocha, S. Kaprzyk and J. Tobola, *Physical Review B*, 2015, 91, 205201.
17. G. Ding, G. Gao and K. Yao, *arXiv preprint arXiv:1505.02477*, 2015.
18. M. Parenteau and C. Carlone, *Physical Review B*, 1990, 41, 5227.
19. D. J. Singh, *Functional Materials Letters*, 2010, 3, 223-226.
20. P. Hohenberg and W. Kohn, *Physical review*, 1964, 136, B864.
21. P. Blaha, K. Schwarz, G. Madsen, D. Kvasnicka and J. Luitz, *An augmented plane wave+ local orbitals program for calculating crystal properties*, 2001.
22. J. P. Perdew, K. Burke and M. Ernzerhof, *Physical review letters*, 1996, 77, 3865.
23. D. M. Ceperley and B. Alder, *Physical review letters*, 1980, 45, 566.
24. E. Engel and S. H. Vosko, *Physical Review B*, 1993, 47, 13164.
25. T. J. Giese and D. M. York, *The Journal of chemical physics*, 2010, 133, 244107.
26. G. K. Madsen and D. J. Singh, *Computer Physics Communications*, 2006, 175, 67-71.
27. O. Løvvik and Ø. Prytz, *Physical Review B*, 2004, 70, 195119.
28. L. Hedin and B. I. Lundqvist, *Journal of Physics C: Solid state physics*, 1971, 4, 2064.
29. K. Tyagi, B. Gahtori, S. Bathula, A. Srivastava, A. Shukla, S. Auluck and A. Dhar, *Journal of Materials Chemistry A*, 2014, 2, 15829-15835.
30. K. Tyagi, B. Gahtori, S. Bathula, S. Auluck and A. Dhar, *Applied Physics Letters*, 2014, 105, 173905.
31. S. Chen, K. Cai and W. Zhao, *Physica B: Condensed Matter*, 2012, 407, 4154-4159.
32. X. Guan, P. Lu, L. Wu, L. Han, G. Liu, Y. Song and S. Wang, *Journal of Alloys and Compounds*, 2015, 643, 116-120.
33. B. Gahtori, S. Bathula, K. Tyagi, M. Jayasimhadri, A. Srivastava, S. Singh, R. Budhani and A. Dhar, *Nano Energy*, 2015.

34. S. Bathula, J. Mula, B. Bhasker, N. K. Singh, K. Tyagi, A. K. Srivastava and A. Dhar, *Nanoscale*, 2015.
35. B. Gahtori, S. Bathula, K. Tyagi, M. Jayasimhadri, A. Srivastava, S. Singh, R. Budhani and A. Dhar, *Nano Energy*, 2015, 13, 36-46.
36. S. Bathula, M. Jayasimhadri, B. Gahtori, N. K. Singh, K. Tyagi, A. K. Srivastava and A. Dhar, *Nanoscale*, 2015, 7, 12474-12483.
37. S. Bathula, M. Jayasimhadri, N. Singh, A. Srivastava, J. Pulikkotil, A. Dhar and R. Budhani, *Applied Physics Letters*, 2012, 101, 213902.
38. S. Fan, J. Zhao, J. Guo, Q. Yan, J. Ma and H. H. Hng, *Applied Physics Letters*, 2010, 96, 182104-182104-182103.
39. L.-D. Zhao, B.-P. Zhang, J.-F. Li, M. Zhou, W.-S. Liu and J. Liu, *Journal of Alloys and Compounds*, 2008, 455, 259-264.
40. G. Anstis, P. Chantikul, B. R. Lawn and D. Marshall, *Journal of the American Ceramic Society*, 1981, 64, 533-538.
41. F. Ren, B. D. Hall, J. E. Ni, E. D. Case, J. Sootsman, M. G. Kanatzidis, E. Lara-Curzio, R. M. Trejo and E. J. Timm, 2007.
42. G. J. Snyder and T. S. Ursell, *Physical review letters*, 2003, 91, 148301.
43. P. H. Ngan, D. V. Christensen, G. J. Snyder, L. T. Hung, S. Linderoth, N. V. Nong and N. Pryds, *physica status solidi (a)*, 2014, 211, 9-17.
44. K. Tyagi, B. Gahtori, S. Bathula, M. Jayasimhadri, S. Sharma, N. K. Singh, D. Haranath, A. Srivastava and A. Dhar, *Solid State Communications*, 2015, 207, 21-25.
45. K. Tyagi, B. Gahtori, S. Bathula, V. Toutam, S. Sharma, N. K. Singh and A. Dhar, *Applied Physics Letters*, 2014, 105, 261902.
46. J. R. Salvador, J. Yang, A. A. Wereszczak, H. Wang and J. Y. Cho, *Science of Advanced Materials*, 2011, 3, 577-586.
47. K. Bartholomé, B. Balke, D. Zuckermann, M. Köhne, M. Müller, K. Tarantik and J. König, *Journal of Electronic Materials*, 2014, 43, 1775-1781.
48. F. Ren, H. Wang, P. A. Menchhofer and J. O. Kiggans, *Applied Physics Letters*, 2013, 103, 221907.
49. J. Salvador, J. Yang, X. Shi, H. Wang, A. Wereszczak, H. Kong and C. Uher, *Philosophical Magazine*, 2009, 89, 1517-1534.
50. S. Bathula, B. Gahtori, M. Jayasimhadri, S. Tripathy, K. Tyagi, A. Srivastava and A. Dhar, *Applied Physics Letters*, 2014, 105, 061902.

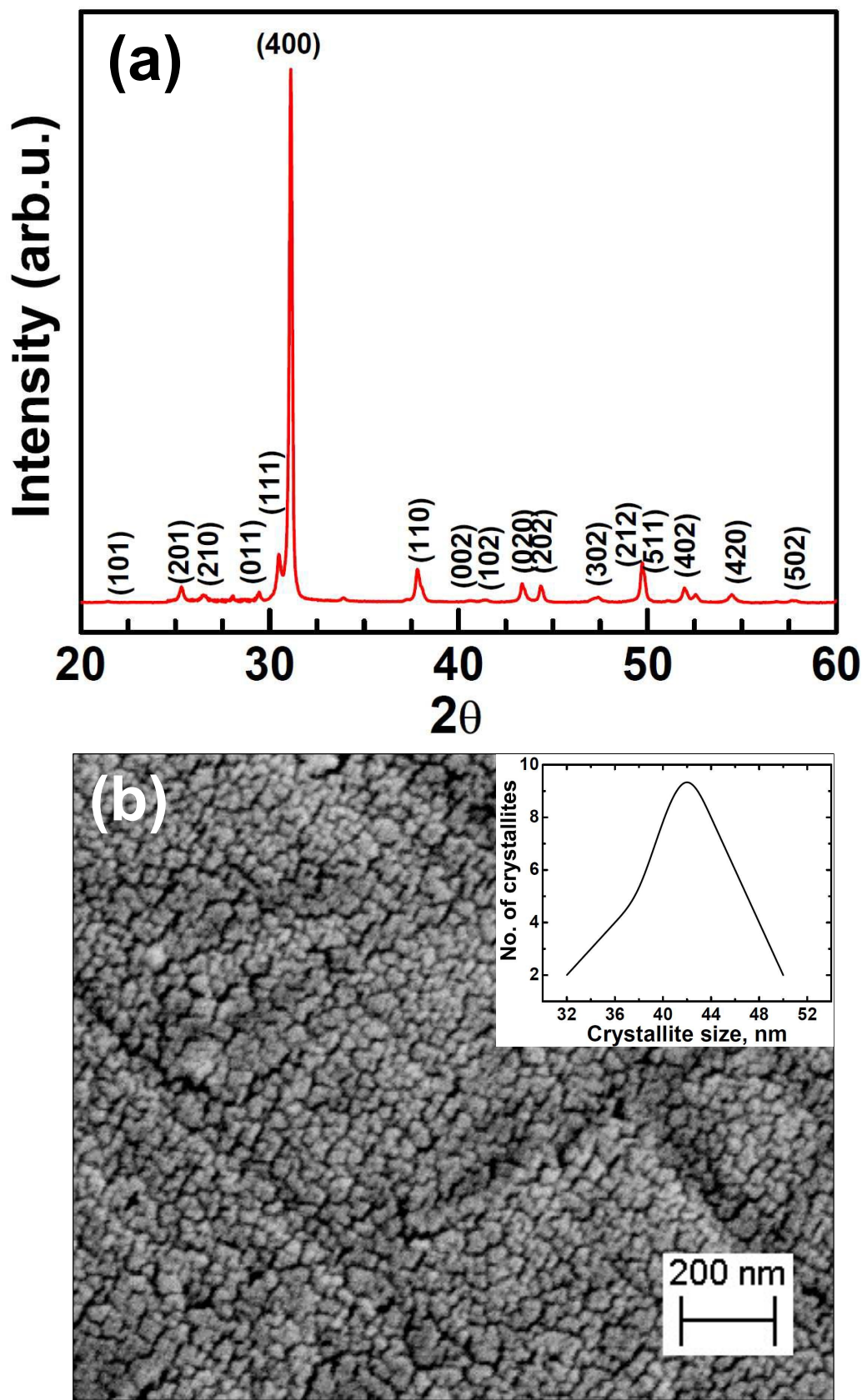


Figure 1

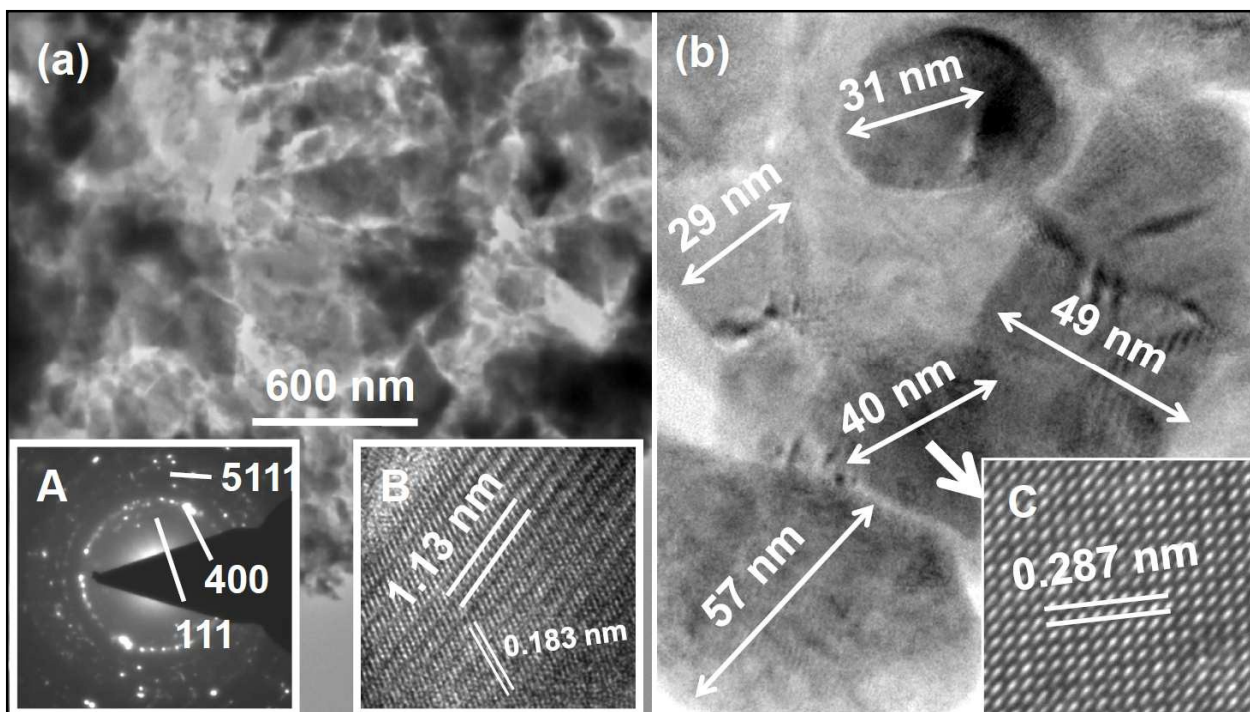


Figure 2

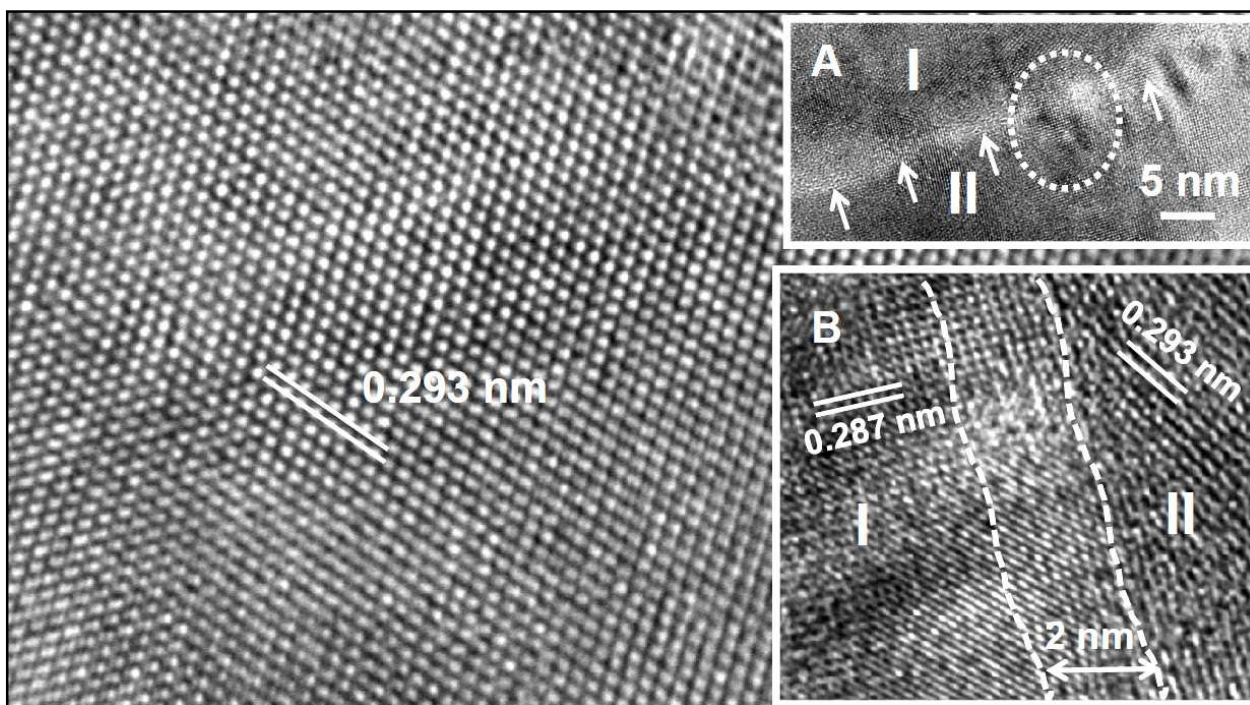


Figure 3

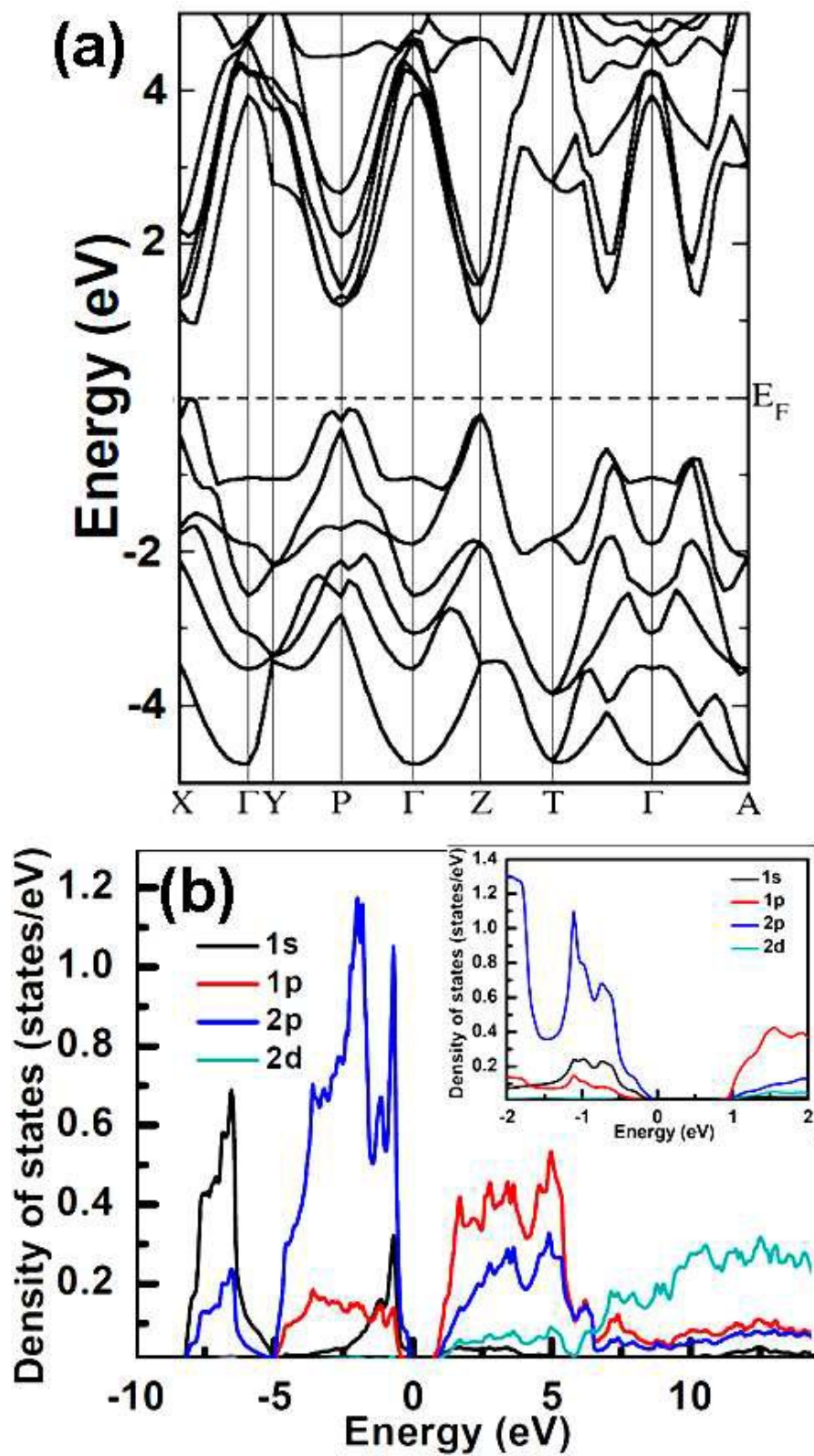


Figure 4

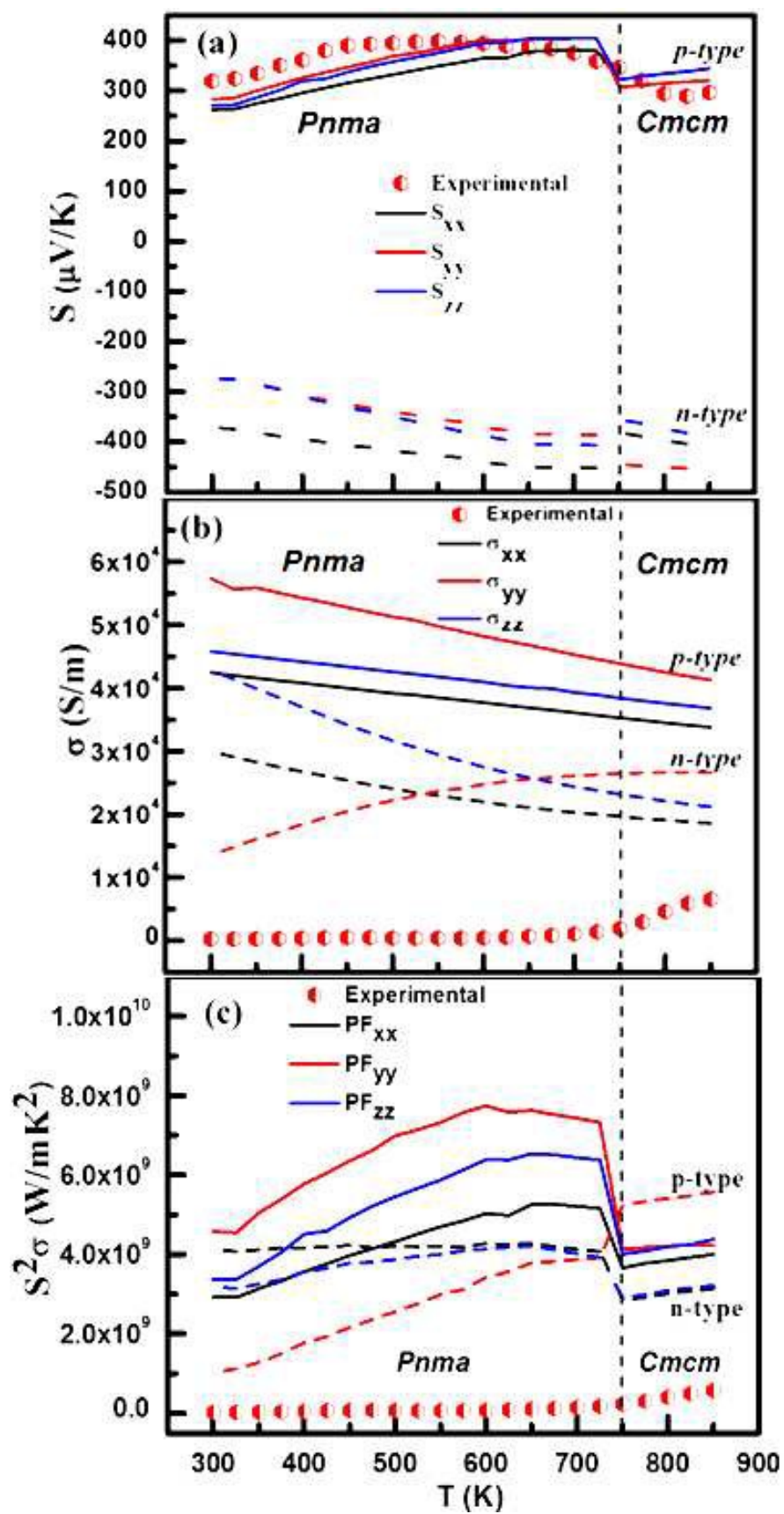


Figure 5

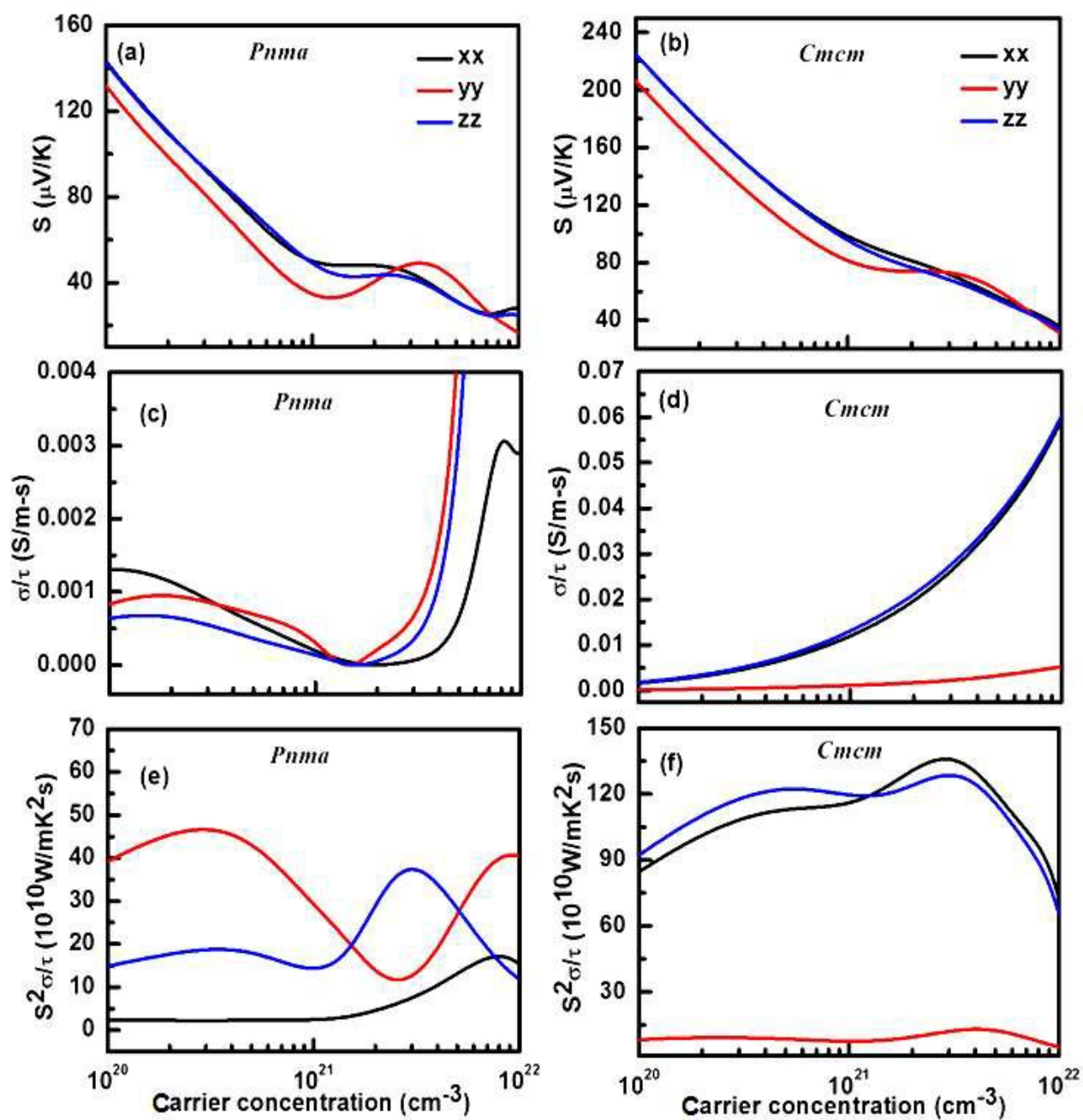


Figure 6